University of Dayton
eCommons

Electrical and Computer Engineering Faculty Publications

Department of Electrical and Computer Engineering

2-2016

Multiclass Object Detection with Single Query in Hyperspectral Imagery Using Class-Associative Spectral Fringe-Adjusted Joint Transform Correlation

Paheding Sidike
University of Dayton

Vijayan K. Asari
University of Dayton, vasari1@udayton.edu

Mohammad S. Alam
University of South Alabama

Multiclass Object Detection with Single Query in Hyperspectral Imagery Using Class-Associative Spectral Fringe-Adjusted Joint Transform Correlation

Paheding Sidike, *Student Member*, *IEEE*, Vijayan K. Asari, *Senior Member*, *IEEE*, and

Mohammad S. Alam, *Fellow*, *IEEE*

Abstract — We present a deterministic object detection algorithm capable of detecting multiclass objects in hyperspectral imagery (HSI) without any training or preprocessing. The proposed method, named class-associative spectral fringe-adjusted joint transform correlation (CSFJTC), is based on joint transform correlation (JTC) between object and non-object spectral signatures to search for a similar match, which only requires one query (training-free) from object's spectral signature. Our method utilizes class-associative filtering, modified Fourier plane image subtraction, and fringe-adjusted JTC technique in spectral correlation domain to perform the object detection task. The output of CSFJTC yields a pair of sharp correlation peaks for a matched target and negligible or no correlation peaks for a mismatch. Experimental results, in terms of receiver operating characteristic (ROC) curves and area-under-ROC (AUROC), on three popular real-world hyperspectral datasets demonstrate the superiority of the proposed CSFJTC technique over other well-known hyperspectral object detection approaches.

Index Terms — Hyperspectral imagery, multiclass object detection, joint transform correlation, fringe-adjusted filter, correlation, class-associative filter, Fourier transforms

I. INTRODUCTION

Hyperspectral imagery (HSI) has been extensively used for object detection and identification applications [1-3] since it provides plenty of spectral information to uniquely identify materials by their reflectance spectra. HSI-based object detection algorithms can be generally classified into stochastic and deterministic approaches. Deterministic approaches are comparatively simple to apply since it is usually based on direct spectral similarity such as spectral angles [4] or spectral correlation [5]. In contrast, stochastic algorithms require statistical modeling and estimation for target class and non-target class [1], or look for pixels that are spectrally distinct from their neighbors without *a priori* information about the target [6]. However, the major challenges associated with stochastic approach is that either adequate data are not available for training samples that account for the target and background spectral characteristics or lacking of sophisticated methods to model the background statistics. Particularly, to make supervised stochastic algorithms perform properly, a great deal of training sets is needed to avoid the well-known Hughes effect [7]. However, training samples are limited and quite difficult to obtain in real-life remote sensing scenarios. Therefore, there is a need for developing a non-training based algorithm to perform object detection tasks. Inspired by this motivation, we herein propose a solution to perform a training-free hyperspectral object detection technique based on joint transform correlation (JTC) [8].

JTC is originally developed for optical pattern recognition, where the reference image and the input scene are introduced in the input plane to create a joint image by use of spatial light modulator (SLM). Then an optical lens $L1$ performs the Fourier transform on the joint image. The intensity of the complex light distribution produced in the back focal plane of $L1$ called joint power spectrum (JPS) which is detected by a square-law device or a liquid crystal light valve (LCLV). In

the final stage of JTC, the resultant JPS is inverse Fourier transformed by a lens $L2$ to yield the correlation output. If the target is present in the input scene, a pair of strong cross-correlation peaks will appear in the output plane. Since the role of $L1$ and $L2$ is to perform Fourier transform and the joint image can be achieved by the addition operation of the reference image and the input image, the optical implementation of JTC can be easily adopted in image processing.

JTC-based algorithms have shown promising results for pattern recognition in two- and three-dimensional image processing applications [9-18]. Among the various JTC techniques, fringe-adjusted JTC (FJTC) [18] appears to be particularly attractive because it avoids the issues otherwise associated with the alternates. To provide an efficient deterministic target detection algorithm in case of HSI, the spectral FJTC (SFJTC) has been proposed in [5]. The SFJTC determines a desired target by analyzing the correlation intensity between an unknown spectral signature and a known reference spectrum and it is able to accommodate noise and certain variations of the spectral signatures compared to alternate deterministic detection algorithms in HSI. To improve the feasibility of the SFJTC, shifted phase-encoded SFJTC has been presented to alleviate the effects of false alarms and other artifacts [19], while the discrete wavelet-based SFJTC, as a supervised training algorithm, has been suggested to make the SFJTC more insensitive to spectral variability [20]. However, all of these techniques were designed to detect only similar patterns (single class objects) in constant time using spectral signature correlation. JTC-based dissimilar pattern detection techniques from two-dimensional image have been introduced in the literatures [21-23] and JTC-based multiclass target detection in HSI has been initiated in [24]. In this paper, we propose a class-associative spectral fringe-adjusted joint transform correlation (CSFJTC) technique for detecting multiclass objects consisting of dissimilar patterns.

In our proposed algorithm, input spectral signatures from a given hyperspectral image data cube are correlated with multiple reference signatures via spectral signature combination and class-associative method [25]. To achieve a better correlation output, the concept of FJTC and the modified Fourier plane image subtraction (FPIS) technique [21, 26] are incorporated in the multiple target detection processes. The output of CSFJTC provides a pair of sharp and high correlation peaks for a match and negligible or no correlation peaks for a mismatch. In other words, if there are desired multiclass patterns are present in the scene, CSFJTC yields distinctive correlation peaks for multiclass objects simultaneously without losing inherent advantages of the SFJTC. Similar to some deterministic target detection approaches, it also does not need any *a priori* training step, whereas in many machine learning techniques, such as support vector machines (SVMs) [27-30] and extreme learning machines (ELMs) [31-33], require the target and non-target information before performing target detection or classification process. Furthermore, CSFJTC employs the decision metric such as peak-to-clutter mean (PCM) [5] to make its output hinged on the signature of the target but not the amplitude. This also enables CSFJTC robust to variations of spectral signature since the reflectance information of a material is usually maintained in HSI whereas the intensity may change due to background noise.

In a nutshell, the proposed method operates using a single pixel spectrum of a similar or dissimilar class of objects to find matches, does not require prior knowledge (learning) about objects or background, and does not require any preprocessing step of a target spectrum.

The main innovative contributions of this paper can be summarized as follows.

1) A class-associative SFJTC technique is developed for object detection in HSI.

2) A deterministic training-free, multiclass object detection algorithm for hyperspectral data is proposed in this paper.

We also conduct a comparative study and investigate the relationship between SFJTC and CSFJTC techniques in hyperspectral target detection. It is shown that they are closely related and essentially equivalent provided that the reference spectral signatures in SFJTC and CSFJTC are the same and input hyperspectral data has negligible noise or large signal-to-noise ratio (SNR).

The rest of this paper is organized as follows: Section II reviews SFJTC algorithm and provides formulation of the proposed method. In Section III, test results are presented and discussed. Finally, Section IV outlines concluding remarks and further directions of this technology.

II. THEORETICAL ANALYSIS

A. *Spectral Fringe-adjusted Joint Transform Correlation (SFJTC)*

The basic concept of SFJTC is derived from the JTC, where a target signal correlated with unknown input signals through Fourier transform process. In case of hyperspectral pattern recognition for a single pixel object, the target signal can be viewed as discrete one-dimensional vector to represent spectral signature. With incorporating the fringe-adjusted filter (FAF) [18] in spectral JTC leads to the SFJTC. To seek the desired targets, all of the pixels spectra in hyperspectral data are individually correlated through the SFJTC process. To mathematically formulate this concept, consider a hyperspectral dataset with M pixels $\{\boldsymbol{s}_i\}_{i=1}^{M}$ in $\mathbb{R}^L$ where L is the number of spectral bands and $\boldsymbol{s}_i = [s_{i1}, s_{i2}, \ldots, s_{iL}]$ represents the ith ($i = 1,2,\ldots,M$) pixel spectrum. Further assume a row vector $\boldsymbol{r} = [r_1, r_2, \ldots, r_L]$ as the reference (pure target) spectral signature and let $\boldsymbol{r}$ and $\boldsymbol{s}_i$ be separated by a distance $2d$ along the x–axis, then the joint spectral signature $\boldsymbol{f}_i$ can be expressed as

$$\boldsymbol{f}_i(x) = \boldsymbol{r}(x + d) + \boldsymbol{s}_i(x - d) \tag{1}$$

Form (1), it can be observed that each pixel vector in hyperspectral data cube is individually jointed to the reference spectrum. Applying the Fourier transform to (1), yields,

$$F_i(u) = |R(u)|\exp[j\phi_r(u) + jud] + |S_i(u)|\exp[j\phi_{s_i}(u) - jud], \tag{2}$$

where $|R(u)|$ and $|S_i(u)|$ are the amplitude; $\phi_r(u)$ and $\phi_{s_i}(u)$ are the phases of the Fourier transform of $r(x)$ and $s_i(x)$, respectively; and u is a frequency-domain variable in x–axis direction. The corresponding JPS can be calculated by

$$\begin{aligned} Y_i(u) &= |F_i(u)|^2 = F_i(u)F_i(u)^* \\ &= |R(u)|^2 + |S_i(u)|^2 + |R(u)||S_i(u)|^* \\ &\times \exp[j\{\phi_r(u) - \phi_{s_i}(u) + 2ud\}] + |R(u)|^*|S_i(u)| \\ &\times \exp[j\{\phi_{s_i}(u) - \phi_r(u) - 2ud\}], \end{aligned} \tag{3}$$

where * denotes complex conjugate, $|R(u)|^2$ and $|S_i(u)|^2$ are the autocorrelation components of $r(x)$ and $s_i(x)$, respectively; and the last two terms are the cross-correlation components between the reference and input signatures. The inverse Fourier transform of the JPS in (3) yields

$$\begin{aligned} y_i(x) &= r(x) \otimes r(x) + s_i(x) \otimes s_i(x) \\ &+ r(x) \otimes s_i(x) * \delta(x + d) + s_i(x) \otimes r(x) * \delta(x - d) \end{aligned} \tag{4}$$

where $\otimes$ and $*$ denote the correlation and convolution operations, respectively. The first two terms in (4) are dc terms, or zero-order diffractions at the origin of the output plane. These terms usually introduce false alarms to the system, thus to avoid this issue, the power spectra of the input signature and the reference signature are subtracted from the JPS. This resultant in the modified JPS, expressed as

$$\begin{aligned} |P_i(u)|^2 &= Y_i(u) - |R(u)|^2 - |S_i(u)|^2 = |R(u)||S_i(u)|^* \\ &\times \exp[j\{\phi_r(u) - \phi_{s_i}(u) + 2ud\}] + |R(u)|^*|S_i(u)| \\ &\times \exp[j\{\phi_{s_i}(u) - \phi_r(u) - 2ud\}] \end{aligned} \tag{5}$$

Performing inverse Fourier transform of the modified JPS, produces two cross-correlation components, given by

$$\boldsymbol{p}_i(x) = \boldsymbol{r}(x) \otimes \boldsymbol{s}_i(x) * \delta(x+d) + \boldsymbol{s}_i(x) \otimes \boldsymbol{r}(x) * \delta(x-d) \tag{6}$$

The performance of the correlation output can be further improved by multiplying the modified JPS with FAF before the final inverse Fourier transform. The FAF is characterized by the transfer function, defined as

$$\boldsymbol{H}(u) = \frac{B(u)}{A(u) + |\boldsymbol{R}(u)|^2} \tag{7}$$

where $A(u)$ and $B(u)$ are either constants or functions of u. When $B(u) = 1$ and $|\boldsymbol{R}(u)|^2 \gg A(u)$, the FAF becomes a perfect inverse filter. The FAF filtered JPS is given by

$$\boldsymbol{G}_i(u) = \boldsymbol{H}(u) \times |\boldsymbol{P}_i(u)|^2 \tag{8}$$

Finally, an inverse Fourier transform of the $G_i(u)$ yields the correlation output as

$$\boldsymbol{g}_i(x) = F^{-1}\{\boldsymbol{H}(u) \times |\mathrm{P}(\boldsymbol{u})|^2\} \tag{9}$$

Assuming that the reference spectrum is the same as the input spectrum, (8) may be rewritten as

$$\boldsymbol{G}_i(u) \approx |\boldsymbol{R}(u)|^{-2} \times |\boldsymbol{R}(u)|^2 [\exp(j2ud) + \exp(-j2ud)]$$

$$\approx \exp(j2ud) + \exp(-j2ud)$$

$$\approx 2\cos(2ud) \tag{10}$$

Consequently, (9) becomes

$$\boldsymbol{g}_i(x) \approx \delta(x+2d) + \delta(x-2d) \tag{11}$$

From (11), it is evident that if the target signal exists in the input scene, SFJTC produces the desired pair of delta-function-like cross-correlation.

B. Proposed Class-associative SFJTC (CSFJTC)

SFJTC can be only performed on single reference (i.e., single class) based target detection tasks, which is incapable of multiclass object detection in HSI. Therefore, we propose a multiclass target

detection strategy, termed as CSFJTC. Block diagram of the CSFJTC algorithm for correlating the input spectral signature with two reference spectra is shown in Fig. 1. To simply illustrate the concept, let us consider two known targets from two classes have unique spectral signatures, denoted as $r_1(x)$ and $r_2(x)$, respectively. Then two joint signatures of $r_1(x)$ and $s_i(x)$ in x-axis direction can be obtained as follows

$$f_{11i}(x) = r_1(x + d) + s_i(x - d) \tag{12-a}$$

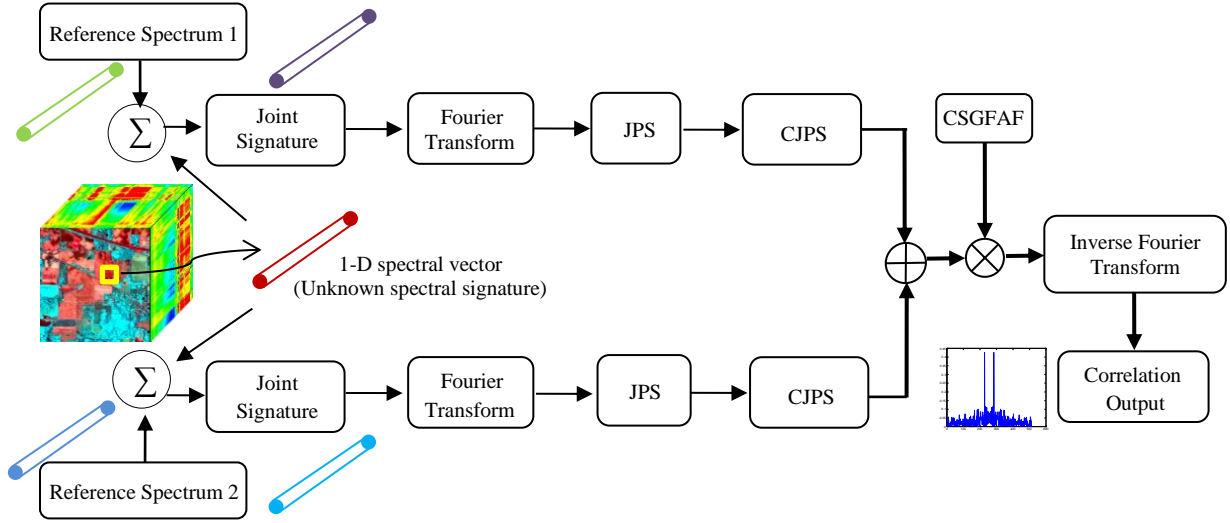$$f_{21i}(x) = r_1(x + d) - s_i(x - d) \tag{12-b}$$

Fig. 1. Block diagram of the proposed pattern recognition scheme for the case of two reference spectra. JPS: Joint Power Spectrum; CJPS: Combination of JPS; CSGFAF: Class-associative Spectral Generalized Fringe-Adjusted Filter.

Similarly, using $r_2(x)$ and $s_i(x)$, another two joint spectral signatures are generated by

$$f_{12i}(x) = r_2(x + d) + s_i(x - d) \tag{13-a}$$

$$f_{22i}(x) = r_2(x + d) - s_i(x - d) \tag{13-b}$$

Applying Fourier Transform to (12) with respect to reference spectrum r_1, we get

$$F_{11i}(u) = |R_1(u)|\exp[j\phi_{r1}(u) + jud] + |S_i(u)|\exp[j\phi_{s_i}(u) - jud] \tag{14-a}$$

$$F_{21i}(u) = |R_1(u)|\exp[j\phi_{r1}(u) + jud] - |S_i(u)|\exp[j\phi_{s_i}(u) - jud] \tag{14-b}$$

where F_{11i} and F_{21i} are the Fourier transform of f_{11i}, f_{21i}, respectively. Similarly, applying

Fourier transform to (13), we obtain

$$F_{12i}(u) = |R_2(u)|\exp[j\phi_{r2}(u) + jud] + |S_i(u)|\exp[j\phi_{s_i}(u) - jud] \tag{15-a}$$

$$F_{22i}(u) = |R_2(u)|\exp[j\phi_{r2}(u) + jud] - |S_i(u)|\exp[j\phi_{s_i}(u) - jud] \tag{15-b}$$

where F_{12i} and F_{22i} are the Fourier transform of f_{12i}, f_{22i}, respectively. The corresponding JPS

to (14) can be computed as follows:

$$T_{11i} = |F_{11i}|^2 = |R_1(u)|^2 + |S_i(u)|^2 + 2|R_1(u)||S_i(u)|\cos[\phi_{r1}(u) - \phi_{s_i}(u) + 2ud] \tag{16-a}$$

$$T_{21i} = |F_{21i}|^2 = |R_1(u)|^2 + |S_i(u)|^2 - 2|R_1(u)||S_i(u)|\cos[\phi_{r1}(u) - \phi_{s_i}(u) + 2ud] \tag{16-b}$$

Likewise, the JPS for (15) are expressed by

$$T_{12i} = |F_{12i}|^2 = |R_2(u)|^2 + |S_i(u)|^2 + 2|R_2(u)||S_i(u)|\cos[\phi_{r2}(u) - \phi_{s_i}(u) + 2ud] \tag{17-a}$$

$$T_{22i} = |F_{22i}|^2 = |R_2(u)|^2 + |S_i(u)|^2 - 2|R_2(u)||S_i(u)|\cos[\phi_{r2}(u) - \phi_{s_i}(u) + 2ud] \tag{17-b}$$

On the right-hand side of (16) and (17), the first two terms corresponding to the zero-order terms,

whereas the third term is the desired cross-correlation between the reference spectrum and the

input spectrum. The zero-order diffractions are due to autocorrelation of the reference spectrum

and the input spectrum, which are responsible for producing false alarms in the JPS. To suppress

the zero-order term and reduce the effects of input-scene noise, the combination of the JPS is

computed as

$$P_{1i}(u) = T_{11i} - T_{21i} = 4|R_1(u)||S_i(u)|\cos[\phi_{r1}(u) - \phi_{s_i}(u) + 2ud] \tag{18}$$

and

$$P_{2i}(u) = T_{12i} - T_{22i} = 4|R_2(u)||S_i(u)|\cos[\phi_{r2}(u) - \phi_{s_i}(u) + 2ud] \tag{19}$$

From (18) and (19), it is evident that the undesired zero-order terms are eliminated simply by

subtraction operation using the JPS of two joint spectral signatures for each reference class, which

can be considered as an alternative approach compared to FPIS, we may term our approach as a modified FPIS (MFPIS). In contrast, SFJTC employs the FPIS technique to eliminate the zero-order terms, where the power spectra of the input signature and the reference signature are subtracted from the JPS as shown in (5). However, the FPIS approach requires the power spectra of the input signature and the reference signature, which introduces complexity for both real-world optical implementation. Therefore, we generate two joint spectral signatures for each reference class to remove the undesired autocorrelation terms and avoid implementation complexity. Comparison of FPIS-based and MFPIS-based CSFJTC will be discussed in Section III-C.

To detect multiple class objects simultaneously, the JPS in (18) and (19) are further combined to achieve equal correlation peaks for both targets and their energy contents are controlled by coefficients a_1 and a_2, such that $a_1 + a_2 = 1$ as

$$
\begin{aligned}
\boldsymbol{P}_i(u) &= a_1 \boldsymbol{P}_{1i}(u) + a_2 \boldsymbol{P}_{2i}(u) \\
&= a_1\{4|\boldsymbol{R}_1(u)||\boldsymbol{S}_i(u)|\cos[\phi_{r1}(u) - \phi_{s_i}(u) + 2ud]\} \\
&\quad + a_2\{4|\boldsymbol{R}_2(u)||\boldsymbol{S}_i(u)|\cos[\phi_{r2}(u) - \phi_{s_i}(u) + 2ud]\}
\end{aligned}
\tag{20}
$$

If there are N classes in the input hyperspectral image, (20) can be rewritten as

$$
\begin{aligned}
\boldsymbol{P}_i(u) &= \sum_j^N a_j \boldsymbol{P}_{ji}(u) \\
&= a_1\{4|\boldsymbol{R}_1(u)||\boldsymbol{S}_i(u)|\cos[\phi_{r1}(u) - \phi_{s_i}(u) + 2ud]\} \\
&\quad + a_2\{4|\boldsymbol{R}_2(u)||\boldsymbol{S}_i(u)|\cos[\phi_{r2}(u) - \phi_{s_i}(u) + 2ud]\} + \cdots \\
&\quad + \ldots + a_N\{4|R_N(u)||\boldsymbol{S}_i(u)|\cos[\phi_{rN}(u) - \phi_{s_i}(u) + 2ud]\}
\end{aligned}
\tag{21}
$$

where $a_1, a_2, \ldots, a_N$ are nonzero coefficients constrained to $\sum_{j=1}^N a_j = 1$. Note that a_1 and a_2 in (20) correspond to the case of two classes. The values of $a_j (j = 1,2, \ldots, N)$ may be varied depending on the energy content of the JPS $\boldsymbol{P}_{ji}$. The study in [21], different values of parameters

a_1 and a_2 for multiclass object detection in 2D imagery is investigated and it is found that the detection performance can be improved by fine tuning these parameters.

In FJTC, the FAF is effectively utilized to suppress the noise spectrum at the Fourier plane. Thus, to produce sharper and larger correlation peak intensity, the FAF filter in (7) is employed and reformulated to a class-associative spectral generalized FAF (CSGFAF), defined as

$$\widetilde{H}(u) = \frac{1}{\epsilon + |\boldsymbol{R}_1(u)|^m + |\boldsymbol{R}_2(u)|^m} \tag{22}$$

where ϵ is a constant which is used to avoid the presence of zero poles that may force the gain of the CSGFAF to approach infinity, thereby creating a serious design problem in realizing this filer. The parameter m is a constant that may be either 0, 1 or 2. Depending on the value of m, CSGFAF in (22) corresponds to the classical matched filter ($m = 0$), phase only filter ($m = 1$), or fringe-adjusted filter ($m = 2$). Thus, all important types of matched filter based correlators can be implemented using the proposed CSGFAF while avoiding the limitations of matched filter based correlators. Previous work in [23] has shown that for an input signal with noise, the phase-only filter ($m = 1$) yields better correlation outputs than the fringe-adjusted filter ($m = 2$). Accordingly, the JPS in (20) can be further enhanced by multiplying the CSGFAF and yields,

$$\widetilde{\boldsymbol{G}}_i(u) = \boldsymbol{P}_i(u) \times \widetilde{\boldsymbol{H}}(u)$$

$$= \frac{[a_1 P_{1i}(u) + a_2 P_{2i}(u)]}{\epsilon + |\boldsymbol{R}_1(u)|^m + |\boldsymbol{R}_2(u)|^m} \tag{23}$$

It is worth to mention that for single class object detection, only one reference spectral signature will be used in CSFJTC. In this case, (23) will be expressed as

$$\widetilde{\boldsymbol{G}}_i(u) = \boldsymbol{P}_i(u) \times \widetilde{\boldsymbol{H}}(u)$$

$$= \frac{a_1 P_{1i}(u)}{\epsilon + |\boldsymbol{R}_1(u)|^m}$$

$$= \frac{a_1\{4|R_1(u)||S_i(u)|\cos[\phi_{r1}(u) - \phi_{s_i}(u) + 2ud]\}}{\epsilon + |R_1(u)|^m} \tag{24}$$

If input and reference spectral signatures are the same and $|R_1(u)|^m \gg \epsilon$ for $m = 2$, then (24)

becomes

$$\widetilde{G}_i(u) \approx 4a_1 \cos(2ud) \tag{25}$$

Finally, applying an inverse Fourier transform to $\widetilde{G}_i(u)$ produces the final correlation output.

For the case of two reference spectral signatures from different class, i.e., $r_1 \neq r_2$, if the input

pixel spectral signature is the same as r_1, the parameter $m = 2$, and for $|R_1(u)|^2, |R_2(u)|^2 \gg \epsilon$,

$\widetilde{G}_i(u)$ in (23) becomes

$$\widetilde{G}_i(u) \approx P_i(u) \times \widetilde{H}(u)$$

$$= 4\frac{a_1 \cos(2ud) + a_2 K_1 \cos[\phi_{r2}(u) - \phi_{s_i}(u) + 2ud]}{1 + K_1^2} \tag{26}$$

where $K_1 = \sum \frac{|R_2(u)|}{|R_1(u)|}$. For $K_1 \ll 1$ and $a_1 = a_2$, $\widetilde{G}_i(u)$ in (26) may be approximated as

$$\widetilde{G}_i(u) \approx 4a_1 \cos(2ud) \tag{27}$$

Similarly, if the input spectrum is the same as r_2, $\widetilde{G}_i(u)$ in (23) becomes

$$\widetilde{G}_i(u) \approx P_i(u) \times \widetilde{H}(u)$$

$$= 4\frac{[a_2 \cos(2ud) + a_1 K_2 \cos[\phi_{r1}(u) - \phi_{s_i}(u) + 2ud]]}{1 + K_2^2} \tag{28}$$

when $K_2 = \sum \frac{|R_1(u)|}{|R_2(u)|}$. For $K_2 \ll 1$ and $a_1 = a_2$, $\widetilde{G}_i(u)$ in (28) may be recomputed as

$$\widetilde{G}_i(u) \approx 4a_2 \cos(2ud) \tag{29}$$

For $K_1 = 1$, i.e., $r_1 = r_2$, using the same parameters as in (26), $\widetilde{G}_i(u)$ may be estimated as

$$\widetilde{G}_i(u) \approx 2[a_1 \cos(2ud) + a_2 \cos(2ud)] \approx 2\cos(2ud) \tag{30}$$

Accordingly, the same result can be obtained for (26) when $K_2 = 1$. From (27), (29) and (30), it is observed that an inverse Fourier transform of the $\widetilde{\boldsymbol{G}}_i(u)$ will generate a pair of delta-function-like cross-correlation peaks indicating the presence of a target. In addition, comparing (10), (25) with (30), it can be seen that SFJTC and CSFJTC yield similar outputs when input targets are same as the reference spectral signature. However, here we assume that signal-to-noise ratio (SNR) is large enough or noise can be negligible.

Study in [5] has shown that the highest value of the correlation output does not yield reliable decision for target discrimination. This is because the correlation peak intensity (CPI) from false signals may have very close value with that from true signals in the correlation plane. Therefore, to avoid false target detection, we utilizes PCM instead of CPI to identify the targets. PCM corresponding for ith pixel spectrum is defined as

$$PCM \quad = \quad \left(\frac{CPI}{L-1} \sum_{\tilde{g}_i \neq CPI} \widetilde{\boldsymbol{g}}_i(x) \right) \tag{31}$$

where $\widetilde{\boldsymbol{g}}_i(x)$ is the inverse Fourier transform of $\widetilde{\boldsymbol{G}}_i(u)$ in (30), and L represents the half length of the correlation output vector. If the target presents in the input image, the final correlation output in the half correlation plane will produce the desired delta-function-like correlation peak at the location of the target in the scene.

The performance of the proposed technique can also be quantified in terms of the true positive rate (TPR) and false positive rate (FPR), which are defined as

$$TPR = \frac{\sum t_p}{\sum t_p + \sum f_n} \tag{32}$$

and

$$FPR = \frac{\sum f_p}{\sum f_p + \sum t_n} \tag{33}$$

where t is the target pixel as per the truth mask, t_p is the target pixel detected correctly (true positive), f_p is the false alarm target pixel (false positive), t_n is background pixel detected correctly (true negative), and f_n is the false background pixel (false negative).
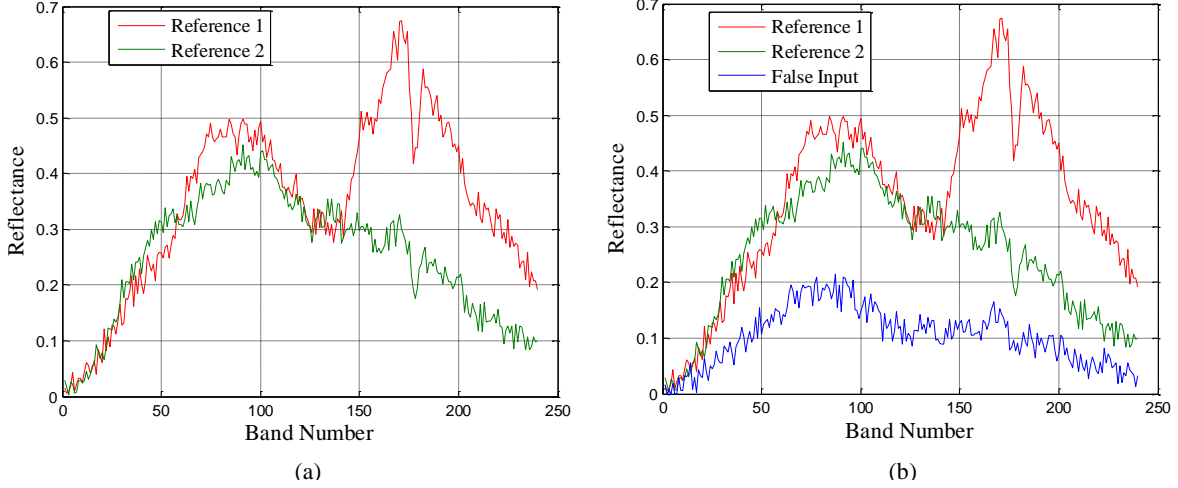
Fig. 2. (Color online) Reference and input spectral signatures. (a) Reference 1 and reference 2 spectral signatures. (b) Reference 1 and reference 2 with a false input.

To illustrate a correlation output of CSJTC based on the analysis above, we correlate two known reference spectral signatures with three input spectral signatures as shown in Figs. 2(a) and 2(b), respectively. Figure 2(a) shows two known reference signals, whereas Fig. 2(b) shows the unknown input spectral signal is dissimilar with either the reference signal 1 or the reference signal 2 which may be considered as a non-target object or false input. The corresponding correlation outputs of the CSFJTC are shown in Fig. 3, where y-axis indicates the correlation intensity, i.e., CPI. From this figure, it is evident that CSFJTC yields a pair of distinct peaks for a matched signal and negligible ones for a mismatch. Table 1 shows quantitative results from Fig. 3 in terms of CPI and PCM metrics. From Table 1, it can be seen that CSFJTC produces much higher CPI and PCM when an input is a true target spectral signature than an input is a false signal. It can also be

observed that PCM provides better discriminability than CPI. Note that the values of CPI and PCM for the two true inputs are not equal. This is due to the energy content of the power spectra of the two reference signals are different. However, we can obtain the desired correlation output by simply adjusting parameters a_1 and a_2.
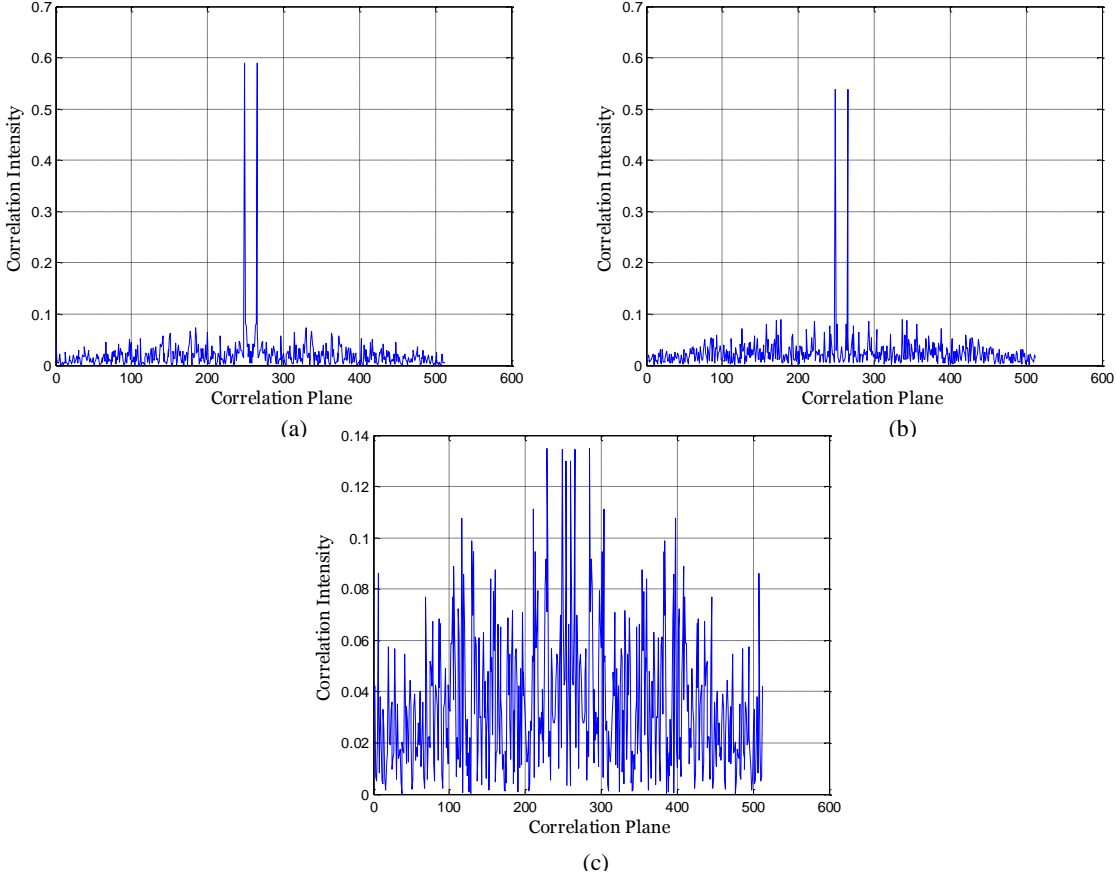
Fig. 3. Correlation outputs with spectral signatures. (a) Correlation output of CSFJTC for an input as reference 1. (b) Correlation output of CSFJTC for an input as reference 2. (c) Correlation output of CSFJTC for a false input as in Fig. 2(b). For parameters in CSFJTC, $a_1 = a_2 = 0.5$ and $m = 2$.

TABLE I
QUANTITATIVE ANALYSIS OF THE CSFJTC OUTPUTS CORRESPONDING TO FIGURES 2 AND 3.

Spectral signatures	Metric	CSFJTC (Fig. 3)
An input as Reference 1	CPI	0.59
	PCM	32.48
An input as Reference 2	CPI	0.54
	PCM	23.63
A false input (Fig. 2(b))	CPI	0.14
	PCM	3.93

III. EXPERIMENTAL RESULTS

In this section, we validate the proposed CSFJTC technique on three commonly used hyperspectral datasets from two aspects. We first evaluate the performance of CSFJTC in single class object detection in HSI, as well as comparisons to other eight competitive hyperspectral target detection algorithms which do not require training. They are adaptive matched filter (AMF) [1], spectral JTC (SJTC) [5], SFJTC [5], spectral angle mapper (SAM) [4], constrained energy minimization (CEM) [34], adaptive cosine/coherent estimator (ACE) [35, 36], spectral information divergence (SID) [37], and Euclidian minimum distance (EMD) [38]. Then we conduct experiments on multiclass object detection tasks with one query in each class of objects as a reference spectral signature for CSFJTC and compare the results with two well-known non-training based multiclass hyperspectral object detectors.

A. Dataset Description and Setups

Three hyperspectral datasets, as described below, are used for testing and evaluation.

Indian Pines: Indian Pines hyperspectral data was acquired by the airborne visible/infrared imaging spectrometer (AVIRIS) over the northwestern Indiana. The image has 220 spectral bands of size 145×145 pixels within spectral range from 0.4 to 2.5μm. There are sixteen mutually exclusive classes considered in this test site. Prior to experiments, twenty water absorption bands are removed, resulting in 200 spectral bands remained. Figure 4 (a) shows the false color composite image and the corresponding ground truth is depicted in Fig. 4 (b).

Salinas: This scene was gathered by 224-band AVIRIS over Salinas Valley, California. The data has a size of 512×217 pixels with a spatial resolution of 3.7-meter per pixel. Twenty water absorption bands (108-112, 154-167, 224) were discarded before experiments. The scene is

covered by vegetables, bare soils and vineyard fields which consists sixteen classes. Figures 5 (a)

and 5 (b) show the corresponding false color composite image and ground truth data, respectively.

The University of Pavia: The University of Pavia test site was collected by the Reflective Optics

System Imaging Spectrometer (ROSIS) over Pavia, northern Italy. The image has 115 bands of

size 610×340 pixels with wavelength ranging from 0.43 to 0.86 µm and is characterized by a

spatial resolution of 1.3-meter per pixel. By removing the noisy bands, the remaining 103 spectral

channels were used in the experiment. Nine land-cover classes were identified as shown in Fig. 6.

(a)   (b)

Alfalfa		Oats	
Corn-notill		Soybean-notill	
Corn-mintill		Soybean-mintill	
Corn		Soybean-clean	
Grass-pasture		Wheat	
Grass-trees		Woods	
Grass-pasture-mowed		Hay-windrowed	
Buildings-Grass-Trees-Drives		Stone-Steel-Towers	
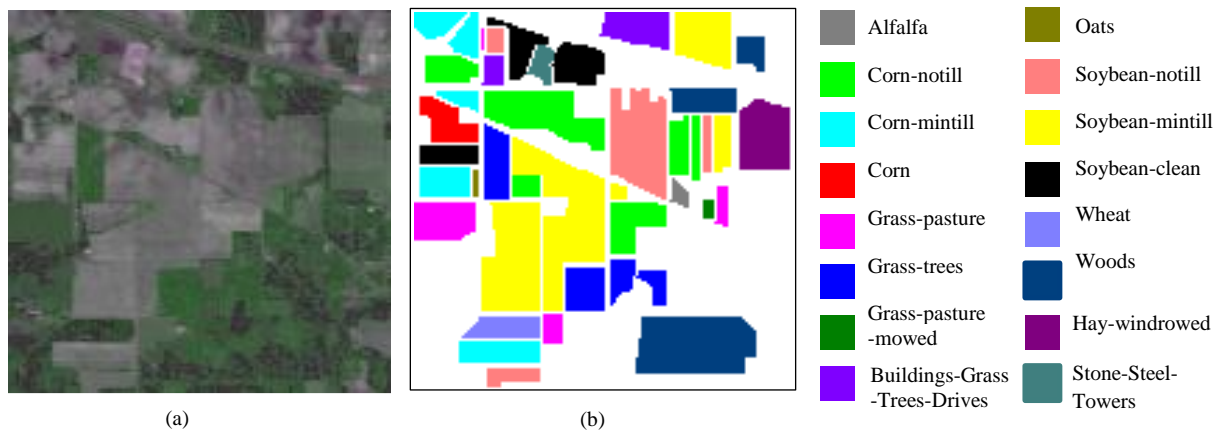
Fig. 4. The Indian Pines dataset. (a) False-color composite. (b) Ground truth.

B. Experiments on Single Class Object Detection

In Section II-B, we have theoretically shown that the proposed CSFJTC algorithm can perform

single object detection tasks by choosing one reference spectral signature for each class at a time.

Similar to SFJTC, CSFJTC is also insensitive to the intensity changes of the reference signature,

since it records the ratio of the highest peak to the clutter mean for the pixel under analysis. We

also concluded that under certain circumstance, SFJCT and CSFJYC will yield approximately the

same results. To examine these remarks, we apply CSFJTC and SFJTC as well as SJTC, AMF,

SAM, CEM, ACE, SID, and EMD on abovementioned three hyperspectral datasets. The detection

results are then compared both visually and quantitatively using receiver operating characteristic (ROC) curves and the corresponding area-under-ROC (AUROC). The ROC curve describes the true positive rate (TPR) as a function of the false positive rate (FPR). The TPR and FPR can be computed as expressed in (32) and (33), respectively.

Experimental Setup: In all experiments, we firstly normalize the input image between 0 and 1. Next, apply maximum noise fraction (MNF) [39] transform, which is also referred to noise-adjusted principal components (NAPC) [40] transform, on the original image as a feature extraction. Compared to principal component analysis (PCA) [41], MNF arranges principal components (PCs) in decreasing order of SNR rather than variance. By retaining the sufficient lower bands in MNF transformed image, we are able to reduce the data dimension and obtain large SNR band images. As mentioned earlier, larger SNR makes the outputs of CSFJTC and SFJTC the same or similar, and MNF transform provides such a stage for this condition. In this experiment, we empirically choose the first 50 bands of MNF transformed image. To convincingly compare and estimate the capabilities of the proposed method with other approaches, we run the experiments ten times with randomly selected reference spectrum for each trial, and ROC and AUROC are averaged over these ten repeated trials.

Parameters Setting: For the parameters of CGFAF in CSFJTC, we select standard values as $\epsilon = 10^{-3}$ and $m = 2$. To demonstrate the similarity of SFJTC and CSFJTC for single class object detection, we use one reference spectral signature in CSFJTC for each class object detection and the JPS coefficient a_j(where $j = 1$ in single class object detection) is set to 1. As for the FAF in SFJTC, we also set $A(u) = 10^{-3}$ and $B(u) = 1$ to have a fair comparison with CSFJTC.

Results and Comparisons: In this section of experiments, since we deal with single class object detection, ROC curve can be generated for each class to visually assess different detection

methods. However, due to large amount of classes in the datasets, it would be inefficient to present all ROC curves here. Thus, we suggest to produce a mean ROC (MROC) curve for each dataset by averaging ROC of each class. Figures 7, 8 ad 9 show the corresponding MROC curves obtained by different methods that tested on Indian Pines, Salinas and University of Pavia datasets, respectively. Qualitatively, the closer to the upper left corner of the plot in ROC curves, the better the performance is. Consequently, a bigger value of AUROC indicates a better outcome.
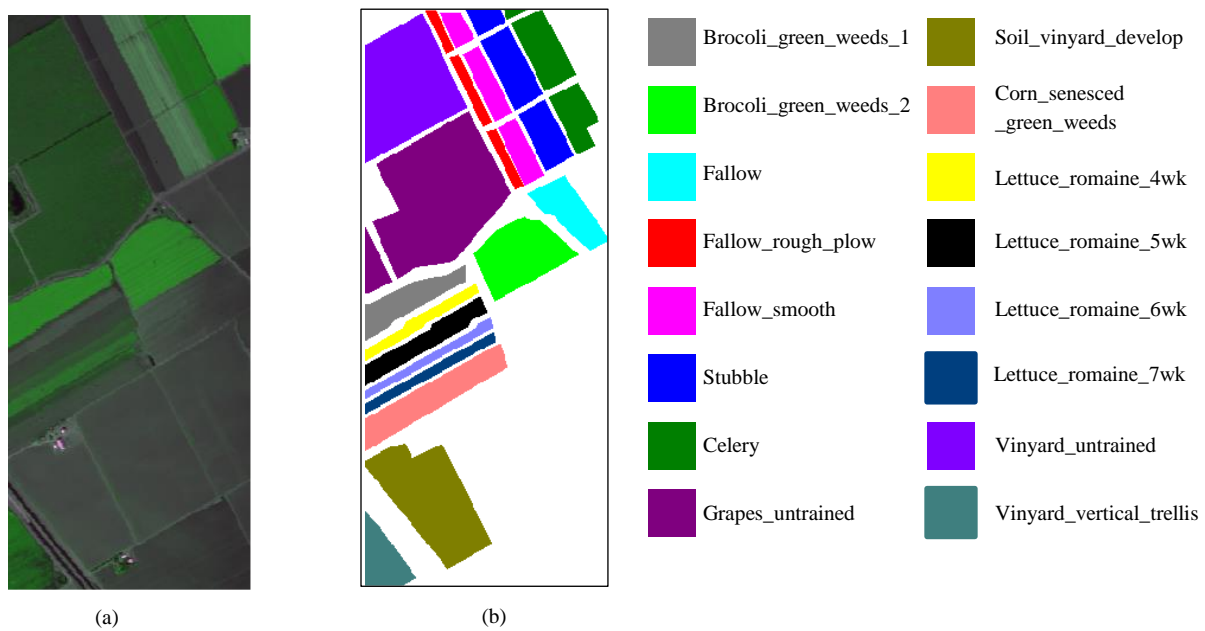

(a) (b)

Fig. 5. The Salinas Scene dataset. (a) False-color composite. (b) Ground truth.
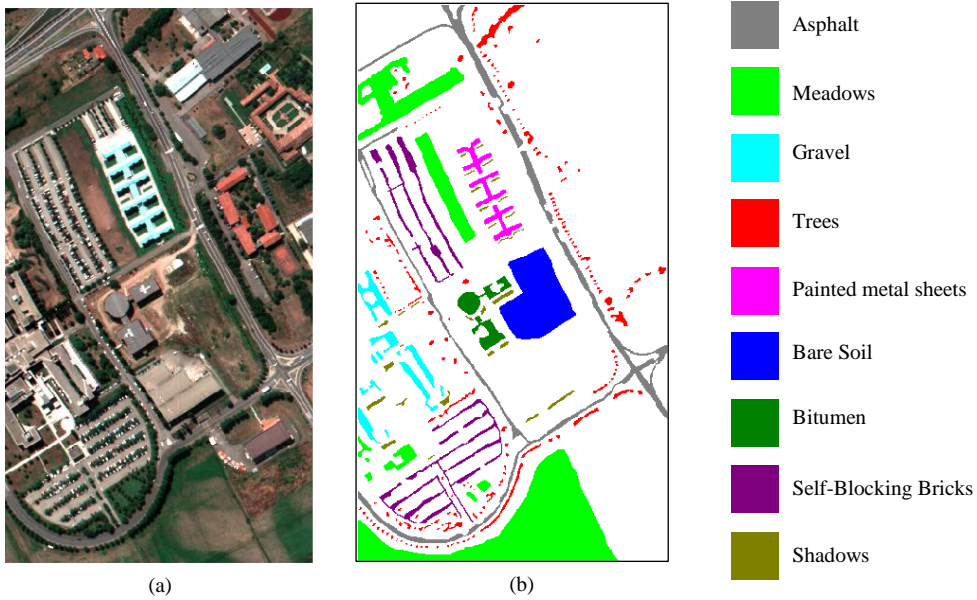
Fig. 6. The University of Pavia dataset. (a) False-color composite. (b) Ground truth.

From test results on the Indian Pines dataset as shown in Fig. 7 and Table II, it is clear that CSFJTC and SFJTC have superior performance than the other approaches. It is worth noting that CSFJTC and SFJTC have identical results, so their ROC curves in Fig. 7 are overlapped, which makes the plot for SFJTC is not visible in this figure and also the other similar figures. Table II reports the corresponding AUROC of various detection algorithms for each class in the dataset. The bold numbers in the table denote the greatest performance among all detectors. From this table, it can be observed that both SFJTC and CSFJTC provide highest AUROC in nine out of sixteen classes and thus yield best results when considering the average AUROC. Comparing AMF with CEM, it is not surprising to discover that they have very similar outputs. This is due to the fact that the AMF is essentially a mean-centered version of CEM, except that AMF uses the covariance matrix instead of the correlation matrix used in CEM.

Figure 8 depicts MROC curves for the Salinas dataset and Table III exhibits the corresponding AUROC for the sixteen types of land-cover classes. Similar to the results obtained from the

experiments on the Indian Pines image, CSFJTC and SFJTC outperform the other methods in terms of AUROC. Moreover, from ROC curves provided in Fig. 8, we observe that for any given false positive rate, CSFJTC and SFJCT produce higher true positive rate than the other techniques, indicating their effectiveness.

Test results on the University of Pavia dataset are shown in Fig. 9 and Table IV. From the ROC plots in Fig. 9, it is obvious that the proposed algorithm along with SFJTC still achieve stellar detection results, this is also verified in Table III in terms of AUROC. Comparing test results on this image with previous two datasets, most detectors including ACE, CEM, AMF, SID, SFJTC and CSFJTC yield lower AUROC, this may be because of heavier spectral variability and large amount of pixel mixture happened in this test site.

Performance of the aforementioned detectors can be further analyzed in terms of their mathematical formulation, such as deterministic or statistic based measure. Deterministic target detection techniques, such as SAM, calculate the spectral similarity value between an input spectral signature and target spectral signatures using only spectral vectors, which is effective only if the spectral signature vectors to be compared are pure signatures of the materials. Accordingly, if a target signature vector is either mixed by other substances such as background signatures (non-target signatures) or embedded in a single signature as a subpixel target, the deterministic approach may fail in target determination and produce false alarms. These obstacles can be partially resolved by statistical approaches, such as ACE which is capable of detecting subpixel targets. This echoes with results from Tables II, III, IV where statistical approaches yields better detection results than deterministic ones due to mixed spectral signatures may occur in the input datasets. However, many statistical models, such as AMF and ACE, assume the background as a multivariate normal distribution, which requires covariance matrices should be calculated over normally distributed

data region which is not always true in real-world HSI data. Even though CEM as subpixel detector is not based on assumption of background statistics, it is found to be very sensitive to noise [42]. Furthermore, it is worth to noting that although the proposed CSFJTC is a deterministic target detection algorithms, it even outperforms the abovementioned statistic based methods. This is because CSFJTC is not a simple step process to measure similarity of spectral signatures, but it involves multiple stages to aid target determination, such as JPS subtraction and fringe-adjusted filtering which play significant roles in accommodating corrupted spectral signatures.
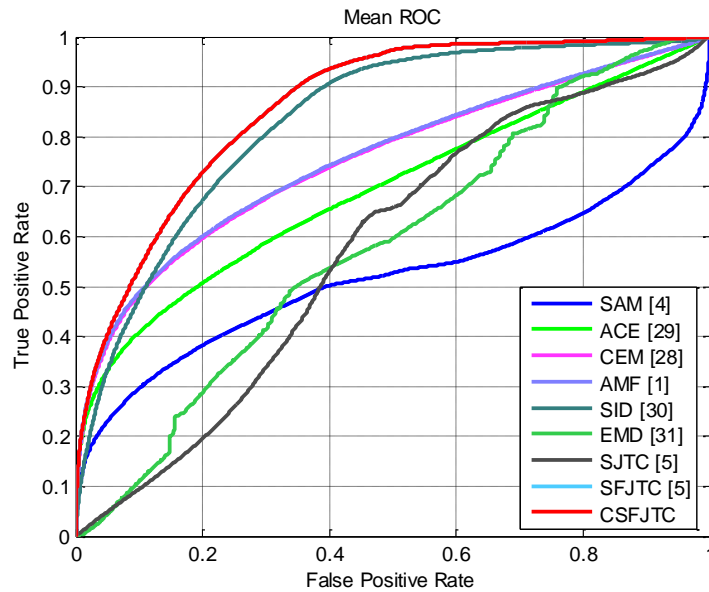

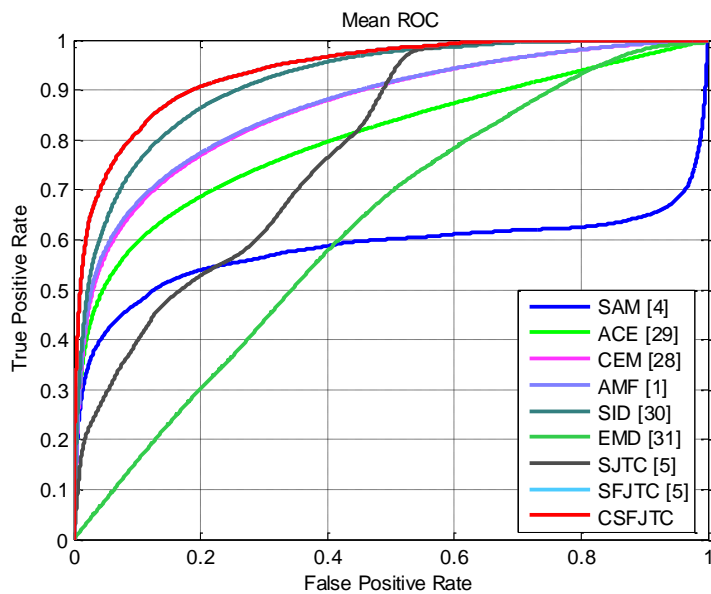Fig.7. MROC for the Indian Pines dataset.
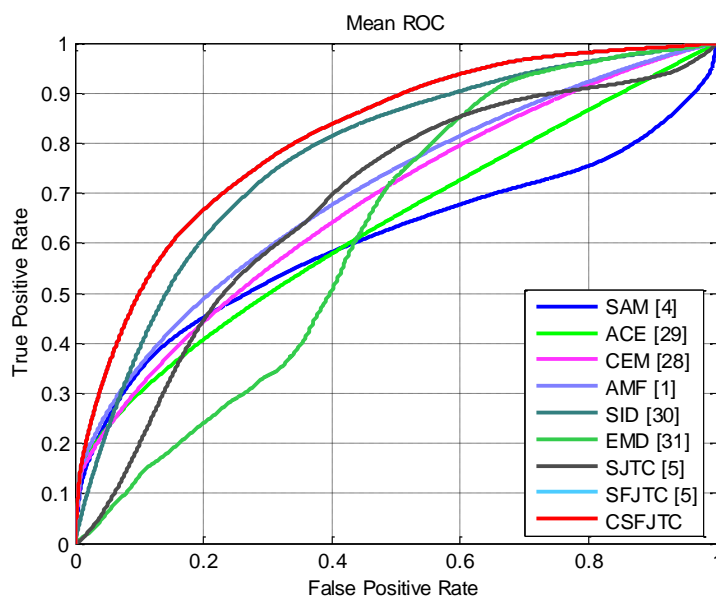
Fig.8. MROC for the Salinas dataset.

Fig.9. MROC for the University of Pavia dataset.

TABLE II
AUROC COMPARISONS FOR THE INDIAN PINES DATASET

Class	Samples	Methods								
		SAM	ACE	CEM	AMF	SID	EMD	SJTC	SFJTC	CSFJTC
Alfalfa	46	0.401	0.868	0.923	0.929	0.891	0.326	0.578	**0.936**	**0.936**
Corn-notill	1428	0.431	0.539	0.598	0.602	0.829	0.601	**0.889**	0.839	0.839
Corn-mintill	830	0.567	0.625	0.685	0.685	0.858	**0.879**	0.768	0.866	0.866
Corn	237	0.651	0.536	0.614	0.616	0.764	**0.926**	0.666	0.833	0.833
Grass-pasture	483	0.626	0.703	0.710	0.713	0.665	**0.791**	0.265	0.716	0.716
Grass-trees	730	0.591	0.720	0.758	0.767	0.756	0.614	0.392	**0.790**	**0.790**
Grass-pasture-mowed	28	0.416	0.931	0.969	0.967	0.932	0.248	0.598	**0.971**	**0.971**
Hay-windrowed	478	0.602	0.767	0.877	0.875	0.921	0.099	0.608	**0.958**	**0.958**
Oats	20	0.597	0.812	0.888	0.887	0.942	0.849	0.438	**0.955**	**0.955**
Soybean-notill	972	0.362	0.562	0.624	0.622	0.828	0.473	**0.847**	0.835	0.835
Soybean-mintill	2455	0.491	0.565	0.636	0.635	0.833	0.592	**0.887**	0.863	0.863
Soybean-clean	593	0.445	0.540	0.638	0.638	0.775	0.722	0.739	**0.781**	**0.781**
Wheat	205	0.490	0.893	0.908	0.931	0.918	0.772	0.347	**0.942**	**0.942**
Woods	1265	0.487	0.613	0.662	0.665	0.868	0.251	0.077	**0.910**	**0.910**
Buildings-Grass-Trees-Drives	386	0.600	0.560	0.624	0.622	0.703	0.518	0.338	**0.742**	**0.742**
Stone-Steel-Towers	93	0.515	0.846	0.929	**0.938**	0.842	0.680	0.737	0.866	0.866
Average AUROC		0.517	0.693	0.753	0.756	0.833	0.584	0.573	**0.863**	**0.863**

TABLE III
AUROC COMPARISONS FOR THE SALINAS DATASET

Class	Samples	Methods								
		SAM	ACE	CEM	AMF	SID	EMD	SJTC	SFJTC	CSFJTC
Brocoli_green_weeds_1	2009	0.501	0.985	0.994	0.994	0.993	0.820	**0.998**	0.995	0.995
Brocoli_green_weeds_2	3726	0.597	0.888	0.938	0.948	0.980	0.373	0.956	**0.990**	**0.990**
Fallow	1976	0.741	0.677	0.786	0.785	0.829	0.174	0.651	**0.870**	**0.870**
Fallow_rough_plow	1394	0.500	0.862	0.904	0.915	0.939	0.561	0.507	**0.991**	**0.991**
Fallow_smooth	2678	0.303	0.745	0.834	0.842	0.951	0.483	0.660	**0.989**	**0.989**
Stubble	3959	0.599	0.948	0.980	0.981	0.996	0.370	0.630	**0.997**	**0.997**
Celery	3579	0.306	0.971	0.981	0.986	0.979	0.229	0.969	**0.983**	**0.983**
Grapes_untrained	11271	0.762	0.605	0.726	0.723	0.901	0.742	0.932	**0.938**	**0.938**
Soil_vinyard_develop	6203	0.311	0.602	0.717	0.717	0.890	0.746	0.823	**0.953**	**0.953**
Corn_senesced_green_weeds	3278	0.571	0.679	0.770	**0.777**	0.740	0.728	0.508	0.761	0.761
Lettuce_romaine_4wk	1068	0.764	0.966	**0.981**	**0.981**	0.929	0.772	0.541	0.938	0.938
Lettuce_romaine_5wk	1927	0.553	0.576	0.671	0.670	**0.874**	0.755	0.578	0.870	0.870
Lettuce_romaine_6wk	916	0.698	0.915	0.951	0.954	0.989	0.730	0.993	**0.995**	**0.995**
Lettuce_romaine_7wk	1070	0.676	0.942	**0.969**	**0.969**	0.890	0.735	0.963	0.946	0.946
Vinyard_untrained	7268	0.851	0.579	0.689	0.690	0.917	0.850	0.904	**0.938**	**0.938**
Vinyard_vertical_trellis	1807	0.577	0.915	0.947	**0.950**	0.895	0.897	0.884	0.906	0.906
Average AUROC		0.582	0.803	0.865	0.868	0.918	0.623	0.781	**0.941**	**0.941**

TABLE IV
AUROC COMPARISONS FOR THE UNIVERSITY OF PAVIA DATASET

Class	Samples	Methods								
		SAM	ACE	CEM	AMF	SID	EMD	SJTC	SFJTC	CSFJTC
Asphalt	6631	0.630	0.527	0.589	0.600	0.764	0.508	0.792	**0.846**	**0.846**
Meadows	18649	0.566	0.537	0.575	0.585	0.679	0.583	0.549	**0.686**	**0.686**
Gravel	2099	0.598	0.600	0.722	0.721	0.877	0.891	0.877	**0.927**	**0.927**
Trees	3064	0.567	0.621	0.747	0.742	0.883	0.529	0.815	**0.884**	**0.884**
Painted metal sheets	1345	0.694	0.998	**0.999**	**0.999**	0.862	0.586	0.562	0.978	0.978
Bare Soil	5029	0.478	0.522	0.550	0.551	0.573	0.428	0.614	**0.615**	**0.615**
Bitumen	1330	0.723	0.552	0.605	0.634	0.870	0.599	0.867	**0.897**	**0.897**
Self-Blocking Bricks	3682	0.556	0.535	0.606	0.607	0.830	0.770	0.863	**0.891**	**0.891**
Shadows	947	0.628	0.806	0.702	**0.877**	0.636	0.666	0.175	0.608	0.608
Average AUROC		0.604	0.633	0.677	0.702	0.775	0.618	0.680	**0.815**	**0.815**

C. Experiments on Multiclass Object Detection

For single class object detection, SFJTC yields similar performance as CSFJTC as analyzed in Section II theoretically and in Section III-B experimentally. However, SFJTC is incapable of performing multiclass object detection tasks at a time. In contrast, the proposed CSFJTC as a deterministic training-free algorithm possesses such a capability.

As mentioned in Section II-B, FPIS and MPIS are two different approach for reducing the undesired correlation terms. Although we used MPIS in CSFJTC formulation, FPIS can be adopted in CSFJTC. So it would be interesting to use these two approaches to evaluate the performance of CSFJTC on multiclass object detection. Thus, we apply CSFJTC with FPIS and MFPIS to the aforementioned three datasets separately, and the results are compared using AUROC. For single class object detection, we computed AUROC for each class of objects in each dataset, whereas in the case of multiclass object detection, AUROC is computed only one time for all classes in each dataset.

In the following sections, we will discuss the difference between single class and multiclass object detection in CSFJTC, the effects of CSFJTC parameters and MNF bands selection.
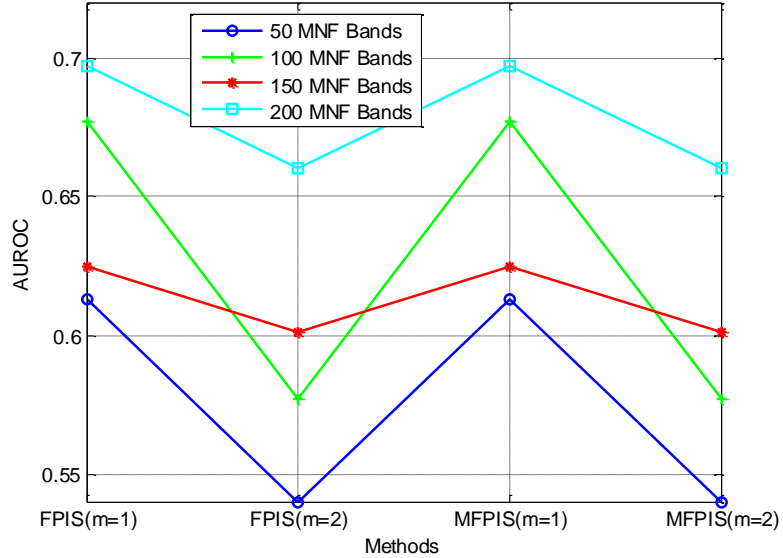
Fig.10. Effects of MNF bands on the Indian Pines dataset.

Differences from single class object detection: There are three major differences between single class and multiclass object detection in the proposed method: 1) Only one reference spectral signature is used in single class objection detection, while N ($N \geq 2$) dissimilar reference spectral signatures (one reference for each class) are used in multiclass object detection which allows for detecting multiple objects from different classes simultaneously. 2) One JPS parameter a_1 is used in single class objection detection, whereas N ($N \geq 2$) such parameters as shown in (21) are used in multiclass object detection where each parameter $a_j (j = 1,2,..,N)$ corresponds to each reference spectral signature related JPS. 3) Formulation of CSGFAF for single class and multiclass object detection is slightly different. For the former one, only two terms (i.e., ϵ and $|R_1(u)|^m$) appear in denominator of CSGFAF, while $N + 1$ terms (i.e., $\epsilon, |R_j(u)|^m j = 1,2,...,N$) are produced in the latter one.

Parameters Setting: For the JPS coefficients $a_j (j = 1,2,...,N)$, we select $a_1 = a_2 = ... = a_N = 1/N$ to have equal weights for each class of JPS, where N is 16 for both Indian Pines and

Salinas datasets, and 9 for The University of Pavia dataset. It is worthy to mention that varying the values of these coefficients may produce slightly different results based on the input dataset. The way to obtain the optimal coefficient will be investigated in our future research direction. As for the parameters m in CSGFAF, we choose $m = 1$ and $m = 2$ to examine their performance.

Effect of Parameter m: For the proposed CSFJTC technique, the selection of parameter m determines the filter types which may also influence the performance. The influence of the parameter m on the detection results for FPIS-based CSFJTC and MFPIS-based CSFJTC are depicted in Figs. 10, 11 and 12, the detailed quantities of corresponding AUROC are summarized in Tables V, VI and VII, respectively. From these results, it can be seen that CSFJTC ($m = 1$) using both FPIS and MFPIS provides the best results for the Indian Pines and the University of Pavia datasets, and yields slightly lower average AUROC for the Salinas dataset than CSFJTC ($m = 2$). Thus, wise choice of the parameter m can achieve greater detection performance. Moreover, it is also observed that FPIS-based CSFJTC and MFPIS-based CSFJTC yield same results for both cases of ($m = 1$) and ($m = 2$), which is expected since FPIS and MFPIS perform similar roles in CSFJTC but different formulation.

However, comparing average AUROC, CSFJTC with $m = 1$ provides the best output, this is due to the fact that there is always an additive amount of noise from various sources (sensor, atmosphere, etc.) in the input hyperspectral image and higher MNF bands contains more noise information, and this causes the joint power spectrum will contain noise terms in forms of autocorrelation of noise itself, cross-correlation between the noise and the reference, and cross-correlation between the noise and the input pixel spectral signature. If we choose $m = 2$ in CSFJTC for the case of N classes, the abovementioned noise terms will be divided by a factor of $\sum_{j=1}^{N}|\boldsymbol{R}_j(u)|^2$, while the factor will be $\sum_{j=1}^{N}|\boldsymbol{R}_j(u)|$ for $m = 1$. Therefore, when $|\boldsymbol{R}_j(u)| \ll 1$, the

effect of noise will be less predominant in $m = 1$. As it is evident in Tables V, VI and VII, $m = 1$ provides better correlation output when more MNF bands (i.e., large noise fraction or smaller SNR) are applied.
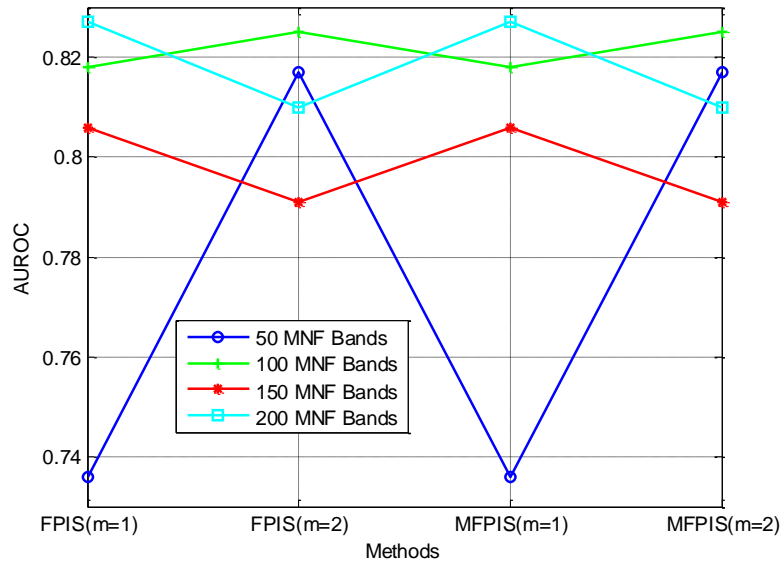

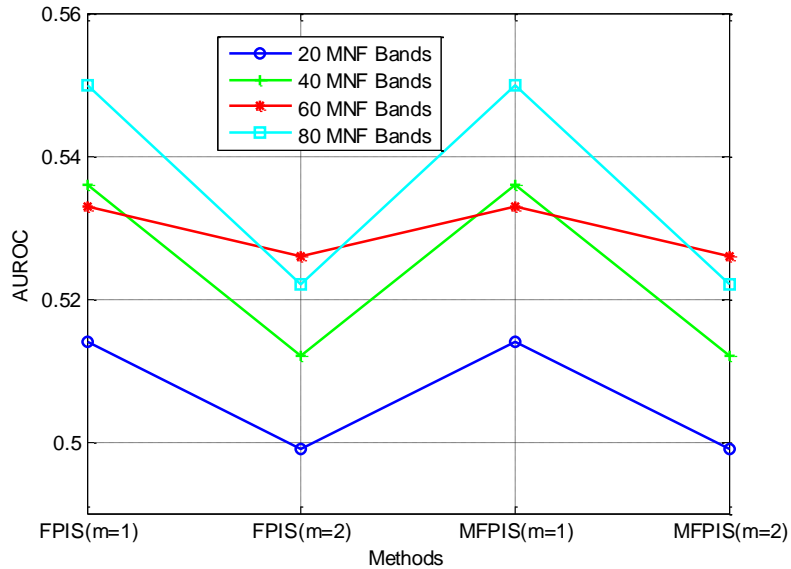Fig. 11. Effects of MNF bands on the Salinas dataset.

Fig. 12. Effects of MNF bands on University Pavia dataset.

Selection of MNF Bands: Similar to experiments in Section III-B, MNF is first applied to the raw images before subsequent processes. For the purpose of multiclass object detection, we randomly select one MNF transformed target spectral signature from each class to represent reference spectral signatures, which is a matrix with a size: (number of target classes) × (dimension of MNF transformed pixel vector). For example, if we use 50 MNF bands for Indian Pines dataset, the reference spectral signatures will be a matrix with size of 16×50.

TABLE V
AUROC COMPARISONS FOR THE INDIAN PINES DATASET

# MNF Bands	Methods			
	CSFJTC-FPIS (m=1)	CSFJTC-FPIS (m=2)	CSFJTC-MFPIS (m=1)	CSFJTC-MFPIS (m=2)
50	0.613	0.540	0.613	0.540
100	0.677	0.577	0.677	0.577
150	0.625	0.601	0.625	0.601
200	0.697	0.660	0.697	0.660
Mean AUROC	**0.653**	0.595	**0.653**	0.595

TABLE VI
AUROC COMPARISONS FOR THE SALINAS DATASET

# MNF Bands	Methods			
	CSFJTC-FPIS (m=1)	CSFJTC-FPIS (m=2)	CSFJTC-MFPIS (m=1)	CSFJTC-MFPIS (m=2)
50	0.736	0.817	0.736	0.817
100	0.818	0.825	0.818	0.825
150	0.806	0.791	0.806	0.791
200	0.827	0.810	0.827	0.810
Mean AUROC	0.797	**0.811**	0.797	**0.811**

MNF transform segregates noise in the data by maximizing SNR. Lower MNF bands typically contain significant information with higher SNR. The amount of spectral information can be adjusted by varying the number of MNF bands. We herein choose various sets of MNF bands to check how the final performance is affected. For the University of Pavia dataset, which has 103

channels, MNF bands 20, 40, 60, and 80 are selected. As for the Indian Pines and Salinas datasets, which have 224 spectral channels, MNF bands 50, 100, 150, and 200 are used.

Figures 10, 11 and 12 illustrate the effects of the MNF bands on the performance of different methods. It can be observed that a better result can be obtained when more MNF bands are used for the case of m = 1. On the other hands, it can be concluded that CSFJTC is sensitive to the number of MNF bands, such as about 9% of improvement can be achieved when using 200 MNF bands compared to 50 bands when m = 1 in the Salinas dataset.

In addition, it is conceded that degraded performance is found for both CSFJTC (m = 1) and CSFJTC (m = 2) in all three testing datasets without MNF transform. The possible reason is that most pixels in hyperspectral imagery are mixed with other substances, such that a target pixel spectrum can be approximated by a linear mixture of its endmember and background (non-target). Consequently, the joint spectral signature will have the noise term, which leads to additional correlation peaks that may yield false alarms.

TABLE VII
AUROC COMPARISONS FOR THE UNIVERSITY OF PAVIA DATASET

# MNF Bands	Methods			
	CSFJTC-FPIS (m=1)	CSFJTC-FPIS (m=2)	CSFJTC-MFPIS (m=1)	CSFJTC-MFPIS (m=2)
20	0.514	0.499	0.514	0.499
40	0.536	0.512	0.536	0.512
60	0.533	0.526	0.533	0.526
80	0.550	0.522	0.550	0.522
Mean AUROC	**0.533**	0.515	**0.533**	0.515

IV. CONCLUSION

In this paper, a new deterministic pattern recognition technique in HSI was proposed. The proposed algorithm is designed to detect multiclass objects consisting of similar and dissimilar

target spectral signatures. Since our method is deterministic, no prior training or complex stochastic analysis is required. This would show the usefulness of the proposed CSFJTC algorithm especially when no sufficient training data are available for performing successful object detection tasks. The obtained results suggest robustness and accuracy of CSFJTC as compared to the other state-of-the-art training-free object detectors in HSI. An observation on the proposed method is that the optimization of filter parameters and selection of MNF dimension will have influence on the object discrimination performance. Test results from multiclass object detection showed that CSFJTC with $m = 1$ yields better outputs than that using $m = 2$, and improved performance can be obtained by using more features from MNF transformed bands. In general, considering all comparison results, we can assess that CSFJTC can be a promising candidate for object detection in hyperspectral remote sensing applications. In our future work, improvements may be achieved by adaptively adjusting JPS coefficients and the parameter m in CSGFAF. Furthermore, integration of spatial and spectral information, and incorporation CSFJTC with neural network for hyperspectral image classification will be investigated.

ACKNOWLEDGMENT

REFERENCES

1. D. Manolakis and G. Shaw, "Detection algorithms for hyperspectral imaging applications," *IEEE Signal Process. Mag.* vol.19, pp. 29–43, Jan. 2002.

2. D. Manolakis, D. Marden, and G. Shaw, "Hyperspectral image processing for automatic target detection applications," *Lincoln Lab. Journal*, vol.14, no.1, pp. 79–114, 2003.

3. H. V. Nguyen, A. Banerjee, R. Chellappa, "Tracking via object reflectance using a hyperspectral video camera," *IEEE Computer Society Conference on Computer Vision and Pattern Recognition Workshops (CVPRW)*, pp.44–51, Jun. 2010.

4. F. A. Kruse, A. B. Lefkoff, J. B. Boardman, K. B. Heidebrecht, A.T. Shapiro, P. J. Barloon, A. F. H. Goetz, "The spectral image processing system (SIPS)—Interactive visualization and analysis of imaging spectrometer data," *Remote Sensing of Environment*, , vol.44, pp. 145–163, 1993.

5. M. S. Alam and S. Ochilov, "Spectral fringe-adjusted joint transform correlation," *Appl. Opt.*, vol.49, no.10, pp. 18–25, Apr. 2010.

6. C.-I Chang, S.-S. Chiang, "Anomaly detection and classification for hyperspectral imagery," *IEEE Transactions on Geoscience and Remote Sensing*, vol.40, no.6, pp.1314–1325, Jun. 2002.

7. G. Hughes, "On the mean accuracy of statistical pattern recognizers," *IEEE Transactions on Information Theory*, vol.14, no.1, pp.55–63, Jan. 1968.

8. C. S. Weaver and J. W. Goodman, "A technique for optically convolving two functions," *Appl. Opt.*, vol.5, pp. 1248–1249, Jul. 1966.

9. L. C. Lin, C. J. Cheng, "Pattern discrimination of joint transform correlator based on wavelet subband filtering," *Optics Communications*, vol. 233, pp. 283–296, April 2004.

10. C. J. Cheng, "Performance of an image-encrypted joint transform correlator for pattern recognition," *Optical Review*, vol. 8, pp. 431–435, Dec. 2001.

11. M. N. Islam, V. K. Asari, M. A. Karim, M. S. Alam, "Distortion-invariant pattern recognition using synthetic discriminant function based multiple phase-shifted-reference fringe-adjusted joint transform correlation," *Optics Communications*, vol. 284, pp. 1532–1539, March 2011.

12. M. R. Haider, M. N. Islam, M. S. Alam, J. F. Khan, "Shifted phase-encoded fringe-adjusted joint transform correlation for multiple target detection," *Optics Communications*, vol. 248, pp. 69–88, April 2005.

13. A. Bal and M. S. Alam, "Dynamic target tracking using fringe-adjusted joint transform correlation and template matching," *Appl. Opt.* vol. 43, pp. 4874–4881, Sept. 2004.

14. M. S. Alam, S. F. Goh, S. Dacharaju, "Three-Dimensional Color Pattern Recognition Using Fringe-Adjusted Joint Transform Correlation With CIELab Coordinates," *IEEE Transactions on Instrumentation and Measurement*, vol.59, no.8, pp. 2176–2184, Aug. 2010.

15. P. Sidike, V. K. Asari, and M. S. Alam, "A robust fringe-adjusted joint transform correlator for efficient object detection," *Proc. SPIE Conference on Defense + Security: Optical Pattern Recognition XXVI*, April 2015.

16. P. Sidike, T. Aspiras, V. K. Asari, and M. S. Alam, "A rotation Invariant pattern recognition using fringe-adjusted joint transform correlation and histogram representation," *Proc. SPIE Conference on Defense + Security: Optical Pattern Recognition XXV*, vol. 9094, pp.90940F, May 2014.

17. P. Sidike, M. S. Alam, C. Cui, and V. K. Asari, "Efficient face recognition using shifted phase-encoded fringe-adjusted joint transform correlator," *Proc. of International Conference on Advances in Electrical Engineering* (ICAEE), pp. 425–430, 2013.

18. M. S. Alam and M. A. Karim, "Fringe-adjusted joint transform correlator," *Appl. Opt*. vol. 32, pp. 4344–4350, Aug. 1993.

19. M. N. Islam, M. S. Alam, "Pattern recognition in hyperspectral imagery using one-dimensional shifted phase-encoded joint transform correlation," *Optics Communications*, vol.281, pp. 4854–4861, Oct. 2008.

20. A. Sakla, W. Sakla, and M. Alam, "Hyperspectral target detection via discrete wavelet-based spectral fringe-adjusted joint transform correlation," *Appl. Opt*., vol. 50, pp. 5545–5554, Oct. 2011.

21. M. S. Alam, and M. M. Rahman, "Class-associative multiple target detection by use of fringe-adjusted joint transform correlation," *Appl. Opt.*, vol. 41, pp. 7456–7463, Dec. 2002.

22. M. R. Haider, M. N. Islam and M. S. Alam, "Enhanced class associative generalized fringe-adjusted joint transform correlation for multiple target detection," *Opt. Eng*. vol. 45, pp. 048201, Apr. 2006.

23. S. M. A. Bhuiyan, M. N. Islam and M. S. Alam, "Distortion-invariant multiple target detection using class-associative joint transform correlation," *Opt. Eng.*, vol. 44, pp. 097201, Sept. 2005.

24. P. Sidike, V. K. Asari and M. S. Alam, "Multiple object detection in hyperspectral imagery using spectral fringe-adjusted joint transform correlator," *Proc. SPIE 9405, Image Processing: Machine Vision Applications VIII*, vol. 9405, pp. 940502, Feb. 2015.

25. J. Khoury, P. D. Gianino and C. L. Woods, "Encoded filter for heterogeneous correlation," *Proc. SPIE* 4043, pp. 225–237, Mar. 2000.

26. M. S. Alam, J. Khan, and A. Bal, "Heteroassociative multiple-target tracking by fringe-adjusted joint transform correlation," *Appl. Opt.* vol. 43, pp. 358–365, 2004.

27. B. E. Boser, I. M. Guyon, and V. N. Vapnik, "A training algorithm for optimal margin classifiers," in *Proc. of the 5th Annual ACM Workshop on Computational learning Theory*, pp. 144–152, 1992.

28. F. Melgani, L. Bruzzone, "Classification of hyperspectral remote sensing images with support vector machines," *IEEE Trans. Geosci. Remote Sens.*, vol.42, pp.1778–1790, Aug. 2004.

29. Y. Bazi, F. Melgani, "Toward an optimal SVM classification system for hyperspectral remote sensing images," *IEEE Trans. Geosci. Remote Sens.*, vol.44, no.11, pp. 3374–3385, Nov. 2006.

30. G. M. Foody, M. Ajay, "A relative evaluation of multiclass image classification by support vector machines," *IEEE Trans. Geosci. Remote Sens.*, vol.42, pp. 1335–1343, Jun. 2004.

31. G.-B. Huang, Q.-Y. Zhu, C.-K. Siew, "Extreme learning machine: Theory and applications," *Neurocomputing*, vol.70, pp. 489–501, Dec. 2006.

32. G.-B. Huang, H. Zhou, X. Ding, R. Zhang, "Extreme learning machine for regression and multiclass classification," *IEEE Trans. Syst. Man Cybern. Part. B*, vol.42, no.2, pp. 513–529, Apr. 2012.

33. M. Pal, A. E. Maxwell, T. A. Warner, "Kernel-based extreme learning machine for remote-sensing image classification," *Remote Sens. Lett.*, vol.4, pp. 853–862, Jun. 2013.

34. J. C. Harsanyi, "Detection and classification of subpixel spectral signatures in hyperspectral image sequences," Ph.D. dissertation, Dept. Elect. Eng., Univ. of Maryland Baltimore County, Baltimore, MD, 1993.

35. S. Kraut, L. L. Scharf, R.W. Butler, "The adaptive coherence estimator: a uniformly most-powerful-invariant adaptive detection statistic," *IEEE Transactions on Signal Processing*, vol.53, no.2, pp.427–438, Feb. 2005.

36. J. Broadwater and R. Chellappa, "Hybrid Detectors for Subpixel Targets," *IEEE Transactions on Pattern Analysis and Machine Intelligence*, vol.29, no.11, pp.1891–1903, Nov. 2007.

37. C.-I. Chang, "Spectral information divergence for hyperspectral image analysis," *IEEE International Geoscience and Remote Sensing Symposium*, vol.1, pp.509–511, 1999.

38. N. Keshava, "Distance metrics and band selection in hyperspectral processing with applications to material identification and spectral libraries," *IEEE Trans. Geosci. Remote Sens.*, vol. 42, pp. 1552–1565, Jul. 2004.

39. A. A. Green, M. Berman, P. Switzer, M. D. Craig, "A transformation for ordering multispectral data in terms of image quality with implications for noise removal," *IEEE Trans. Geosci. Remote Sens.*, vol. 26, no.1, pp. 65–74, Jan. 1988.

40. J. B. Lee, A. S. Woodyatt, and M. Berman, "Enhancement of high spectral resolution remote sensing data by a noise-adjusted principal components transform," *IEEE Trans. Geosci. Remote Sens.*, vol. 28, no.3, pp.295–304, May 1990.

41. I. T. Jolliffe, *Principal Component Analysis*. 2nd ed., New York: Springer-Verlag, 2002.

42. Chang C, Liu J, Chieu B, et al, "Generalized constrained energy minimization approach to subpixel target detection for multispectral imagery," *Opt. Eng.*, vol. 39, pp.1275–1281, 1999.